

Aero-elastic wind tunnel test of a high lighting pole

Yaozhi Luo^{*}, Yucheng Wang, Jiming Xie, Chao Yang and Yanfeng Zheng

College of Civil Engineering and Architecture, Zhejiang University,
866# Yuhangtang Road, Hangzhou, Zhejiang, China

(Received December 17, 2016, Revised June 28, 2017, Accepted June 29, 2017)

Abstract. This paper presents a 1:25 multi-freedom aero-elastic model for a high lighting pole at the Zhoushan stadium. To validate the similarity characteristics of the model, a free vibration test was performed before the formal test. Beat phenomenon was found and eliminated by synthesis of vibration in the X and Y directions, and the damping ratio of the model was identified by the free decay method. The dynamic characteristics of the model were examined and compared with the real structure; the similarity results were favorable. From the test results, the major along-wind dynamic response was the first vibration component. The along-wind wind vibration coefficient was calculated by the China code and Eurocode. When the peak factor equaled 3.5, the coefficient calculated by the China code was close to the experimental result while Eurocode had a slight overestimation of the coefficient. The wind vibration coefficient during typhoon flow was analyzed, and a magnification factor was suggested in typhoon-prone areas. By analyzing the power spectrum of the dynamic cross-wind base shear force, it was found that a second-order vortex-excited resonance existed. The cross-wind response in the test was smaller than Eurocode estimation. The aerodynamic damping ratio was calculated by random decrement technique and the results showed that aerodynamic damping ratios were mostly positive at the design wind speed, which means that the wind-induced galloping phenomenon is predicted not to occur at design wind speeds.

Keywords: high lighting pole; aero-elastic model; wind tunnel experiment; high-rise structure; aerodynamic damping ratios

1. Introduction

High-rise structures can be classified into 3 groups based on the wind-resistant design method: 1. Super high-rise buildings, as shown in Fig. 1(a). When designing this type of building, the user's comfort requirements need to be considered, and wind-induced vibration should be strictly controlled. Therefore, wind-resistant design of these structures is relatively complicated and needs to be carefully demonstrated in detail. 2. High-rise towers such as TV towers and transmission towers, as shown in Fig. 1(b). Wind-resistance analysis still needs to proceed carefully because the complicated shapes of the structures can lead to complicated wind-induced responses. In addition the presence of antennas usually requests serviceability limit state verifications for structural rotations that may put a telecommunication tower out-of-service. 3. Slender high-rise structures such as antenna masts and lighting poles, as shown in Fig. 1(c). These structures have large

^{*}Corresponding author, Professor, E-mail: luoyz@zju.edu.cn

height-width ratios that can reach 50:1 or even 100:1, which can lead to a relatively low natural frequency. Additionally, the cross-section outlines of these structures are relatively simple, and vortex-induced vibration and aerodynamic instability can easily occur.

Many wind tunnel experiments and much theoretical research have been conducted in the past to study and simplify the wind loads on slender high-rise structures. For super high-rise buildings with regular shape and simple cross-section, wind tunnel pressure tests or high frequency force balance (HFFB) tests are effective ways to study the wind load on these structures (Fediw *et al.* 1995, Gu and Quan 2004, Rosa *et al.* 2012). However, designing a rigid model for slender structures such as steel chimneys or lighting poles has proved more difficult. Therefore, theoretical calculation based on quasi-steady assumptions (Caracoglia and Jones 2007, Gorski 2009), free vibration tests on models (Caracoglia and Velazquez 2008) and field measurement tests (Caracoglia 2007, Kawecki and Żurański 2007) may be better ways to study the wind loads and wind-induced vibrations of these structures.



(a) Super high-rise building



(b) High-rise tower



(c) Slender high-rise structure

Fig. 1 Typical high-rise structures

Moreover, the computational fluid dynamics (CFD) technique is also an effective way to study the wind load on these structures. By simplifying aero-dynamic forces during CFD simulation, fluid-solid coupling effects on these structures, such as vortex shedding (Belver *et al.* 2012) and lock-in and drag amplification effects (Belver *et al.* 2012), have been simulated. Additionally, for slender structures with relatively complex shapes, aero-elastic model tests may be a better choice to study the wind effects. Using a full elastic model (Belloli *et al.* 2014) or a separate elastic model (Nguyen *et al.* 2015), wind load characteristics, responses of structures and fluid-solid coupling effects can be carefully studied.

Based on the previously mentioned research, design codes for high-rise structures in different countries have been revised for decades. Currently, design codes for high-rise structure wind loads normally use quasi-steady theory to estimate wind loads and then simplify the method of single degree-of-freedom (DOF) vibration to calculate dynamic responses (Zhou *et al.* 2002). However, for slender structures, such as steel chimneys, the structure response may be underestimated by code calculation (Verboom and Van Koten 2010). Moreover, structure responses in different codes are considerably different. For example, aero-elastic damping is not considered in the China code during the calculation of cross-wind response, which will cause underestimation compared with other codes (Chen *et al.* 2014). Additionally, these structures usually have a relatively small damping ratio (0.1%-1%) because they are mostly one-piece steel structures; therefore, the cross-wind load will be the major wind load on the structures (Gu and Quan 2004). Cross-wind vortex-induced vibration under daily winds can easily cause fatigue failure of basement components (Repetto and Solari 2010). When a structure has a complex cross section, the critical wind speed of wind-induced instability will be significantly decreased, and traditional methods will thus underestimate the wind-induced responses (Nguyen *et al.* 2015). Therefore, existing codes in different countries still cannot accurately estimate wind loads on these complex slender high-rise structures. More importantly, the number of complex slender structures is rapidly increasing because of the development of national public construction in China. Therefore, the study of the wind vibration characteristics of these special high-rise structures is essential.

We conducted a wind tunnel experiment based on a multiple DOF aero-elastic model to examine the structural response and bottom reaction characteristics of a 40 m highlighting pole under strong wind conditions. The high lighting pole is located at Zhoushan in the east of Zhejiang province and close to the East China Sea. The bottom support part of the lighting pole is a circular variable-cross-section steel tube. The cross-section decreases from the 2 m diameter bottom to the 1.3 m top. The upper structure consists of 241 steel tubes; a sketch of the lighting pole is shown in Fig. 2(a). A modal analysis of the structure was conducted using the finite element analysis software. The first four natural frequencies of the structure are 0.817 Hz, 0.82 Hz, 4.351 Hz and 4.695 Hz, and the corresponding modal shapes are first-order mode in the X direction, first-order mode in the Y direction, second-order mode in the X direction and second-order mode in the Y direction, respectively. The coordinate direction is also shown in Fig. 2(a).

2. Wind tunnel experiment

2.1 Aero-elastic model design

Because higher modes of vibration of the lighting pole structure could not be ignored and the structure was too slender for a rigid model, a multiple-DOF aero-elastic model experiment was the

most accurate way to study the wind vibration response of this structure. From the similarity rules based on the Navier-Stokes equations and kinematic equations, if certain critical parameters of the model were similar to those of the actual structure, the measured results of wind-induced vibration in the test would also be similar to those of the actual structure. For this structure, mass distribution and vibration mode are the most critical parameters, but they are difficult to simulate accurately. Because the major responses of concern in this test were the basement bending moment, basement shear force and structure acceleration, we could simplify the similarities of these two parameters into similarities of three simpler parameters

$$m^* = \int_0^H m(z)\phi^2(z)dz \quad (1)$$

$$M^* = \int_0^H m(z)\phi(z)zdz \quad (2)$$

$$F^* = \int_0^H m(z)\phi(z)dz \quad (3)$$

In Eqs. (1)-(3), m^* , M^* and F^* are the generalized mass, base bending moment and base shear force caused by inertia, respectively. $m(z)$ is the unit mass at height z , and $\phi(z)$ is the vibration shape function of the structure.

Because of the height of the real structure and the size of the wind tunnel, the geometric scale ratio during this test was set to 1:25. In this test, the second-order effects of gravity (P- Δ effect) were negligible; therefore, the Froude number of the model did not need to be similar to that of the real structure, which means that the scale of the natural frequency or the scale of the wind speed could be determined at will. Considering the appropriate wind speed range during the test, the preliminary scale of natural frequency was set to 5:1, and the side stiffness and weight distribution of the model were designed based on this scale.

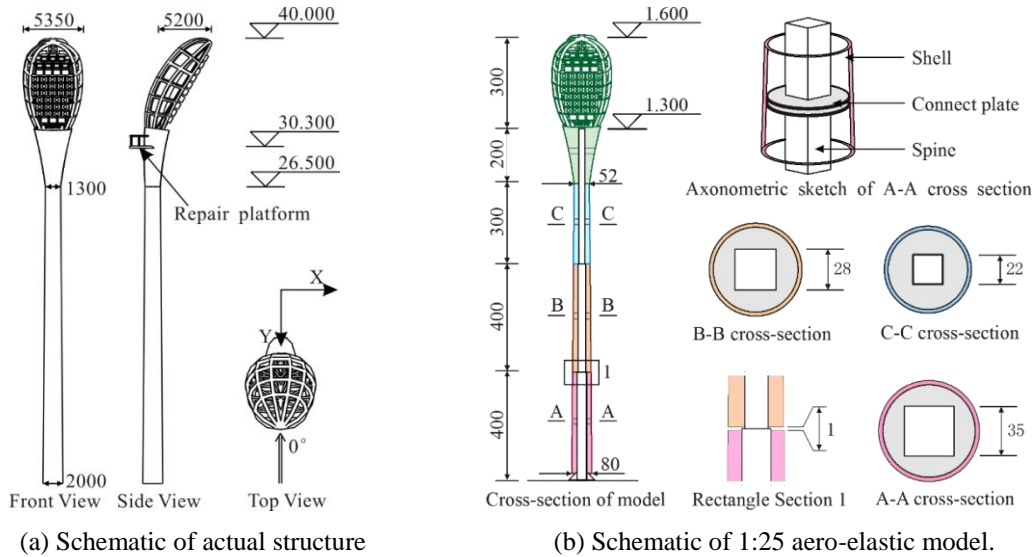


Fig. 2 High lighting pole schematics

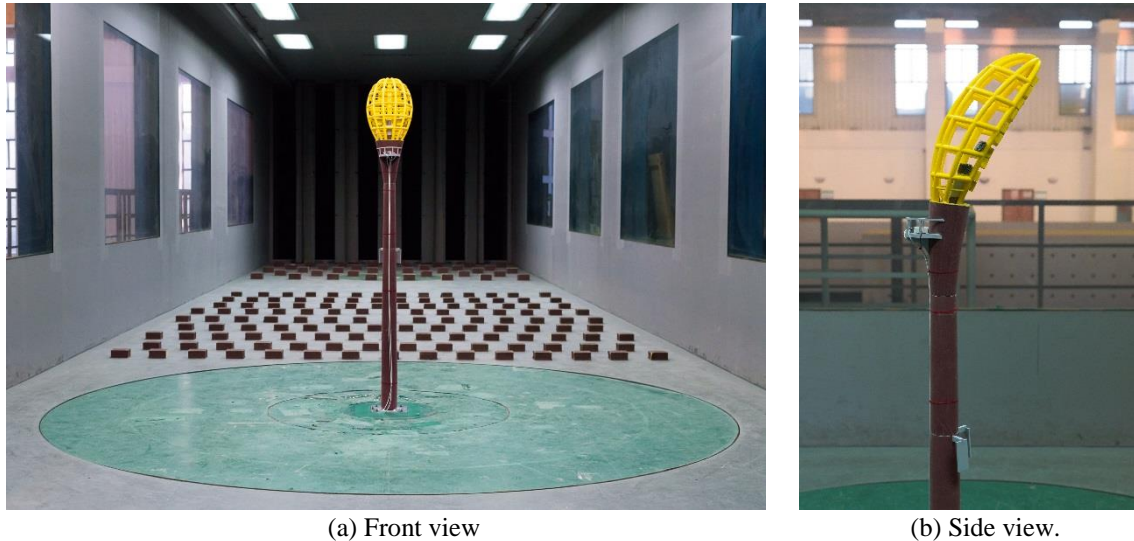


Fig. 3 Appearance of model in wind tunnel

The model used a spine for stiffness, the shell was divided into several parts to simulate the appearance of real structure, and extra weight was added to produce an appropriate weight distribution. The aluminum alloy spine was 1.3 m high and had three sections from bottom to top, as shown in Fig. 2(b). To ensure the stiffness and integrity of the spine, CVC technology was used for completion. The shell had four segments; the size of each segment is shown in Fig. 2(b). Every segment was made by 3D printing and then stuck on the spine with several thin plastic plates. Each segment was separated by a neighbor segment. The space was 1 mm as shown in Fig. 2(b) to ensure that the shell would not provide additional stiffness. To satisfy the mass scale, a 1.2 kg weight was placed on the structure at 1.4 m. Considering the similarity of the Reynolds number, the surface of the cylinder part needed to be properly roughened. In this study, sandpaper was used to cover the surface of the model to simulate the characteristics of the high Reynolds number of the real structure.

To simultaneously measure the wind load and vibration response of the model, this test used an HFFB to measure the reaction force and two acceleration sensors to measure the vibration response of the structure. The range of the HFFB was 260 N/52 N·m, the accuracy was 0.1% FSO, and the sampling frequency was 500 Hz. The range of the acceleration sensor was ± 50 g, the accuracy was 3% FSO, and the maximum sampling frequency was 25 kHz. Two acceleration sensors were perpendicularly placed on the repair platform of the structure as shown in Fig. 2(a). The appearance of the model in the wind tunnel test is shown in Fig. 3.

2.2 Free vibration test

To examine the possible differences between the real model and the theoretical model, a free vibration test for the model was conducted before the formal test. Because the first-order natural frequencies in X direction mode (4.211 Hz) and the one in Y direction mode (4.272 Hz) were very close, beat phenomenon was found during the free vibration test, which is because that these two modes are coupled due to the presence of torsional effects. In other words, the motion in the X

direction gives rise to a component of the motion in the Y direction and vice-versa. Fig. 4 shows an example of vibration time history in the X and Y directions when model was excited in X direction. The X and Y coordinate directions are shown in Fig. 2(a). This phenomenon caused some difficulties for damping ratio identification but it did not affect the identification of vibration frequency.

Based on the spectrum analysis of several test results, the average first four natural frequencies of the model were 4.211 Hz, 4.272 Hz, 23.44 Hz and 23.07 Hz, and the corresponding frequency scales were 5.15, 5.21, 5.39 and 4.91, respectively. The final frequency scale of the model was 5.17:1. The errors of different mode frequency scale were less than 5%, as shown in Table 1, which confirmed that the frequency simulation was accurate. Therefore, the wind speed scale could be calculated by the similarity rule, and the result was 1:4.84.

After determining the frequency of the model, generalized parameters of the model needed to be checked to ensure that the dynamic characteristics of the model were similar to those of the real structure. 5 pairs of accelerometers placed in orthogonal directions were stick on the surface of model at different height: 0.2 m, 0.6 m, 1 m, 1.28 m, 1.6 m. The measured vibration mode in the X direction and the theoretical vibration mode by FEM are shown in Fig. 5; the mode in the Y direction was similar and will not be listed. The simulation of the first-order vibration mode was accurate, although the second-order vibration mode was slightly different from that of the real structure because of the simplification of stiffness distribution.

Table 1 Results of the frequency test

Mode	Theoretical frequency/Hz	Actual frequency/Hz	Scale ratio of frequency	Average ratio	Error
1	4.09	4.21	5.15	5.17	-0.23%
2	4.10	4.27	5.21		0.84%
3	21.76	23.44	5.39		4.28%
4	23.48	23.07	4.91		-4.89%

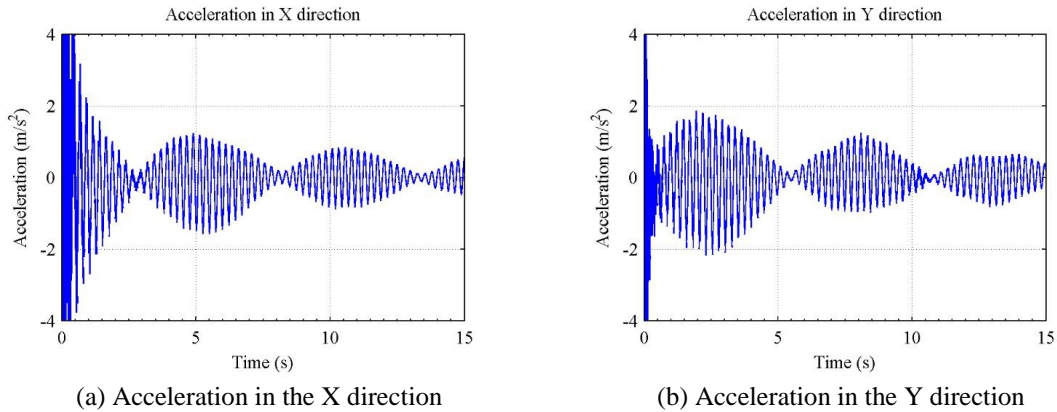


Fig. 4 Time history of acceleration in the vibration test

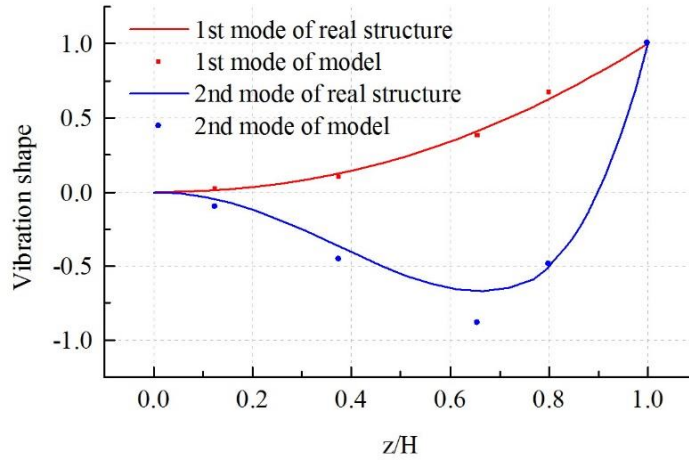


Fig. 5 Results of the vibration mode test in the X direction.

Table 2 Generalized parameter results

Parameter	Mode	Test result	Actual structure result	Error
m^*	1st mode	3.859	3.998	-3.61%
	2nd mode	4.774	4.189	13.97%
M^*	1st mode	4.485	4.616	-2.92%
	2nd mode	1.427	1.276	11.81%
F^*	1st mode	3.528	3.42	3.14%
	2nd mode	2.445	2.068	18.23%

Based on Eqs. (1)-(3) the generalized parameters of the model were calculated and compared with the real structure, as shown in Table 2. The test model was similar in terms of the generalized parameters of the first mode; the errors were all under 5%. The similarity of the generalized parameters of the second mode was reasonable because the vibration shape function was not exactly the same as that of the real structure and because the mass distribution was simplified. Fortunately, although the average errors of the second-order generalized parameters were relatively large (up to 14.67%), the error of each generalized parameter was close to the average error. Therefore, we revised the second-order response in the test results analysis with a uniform value of 14.67%, which means that the error of estimation for each second-order response (vibration acceleration, basement bending moment and basement shear force caused by second-order vibration) was reduced to less than 5%.

As shown in Fig. 4, the beat phenomenon caused some difficulty in damping ratio identification. However, we could reasonably hypothesize that the damping ratios in the X and Y vibration directions should be close to each other. Therefore, we synthesized the vibration in the X and Y directions by vector synthesis and used the time history of acceleration, shear force and bending

moment to identify the damping ratio. The identification results were relatively stable, and the damping ratio was 0.0032 on average, as shown in Table 3. This ratio is lower than full-scale measurements result of a 30 m lighting pole 0.01~0.08 (Pagnini and Solari 2001), but the lower value is in accordance with the U.S. code 0.002~0.006 (ASME 2006) and Europe code 0.0019~0.006 (Eurocode 2006). Moreover, a smaller damping ratio would be helpful to observe the aerodynamic effects of the structure and would lead to a relatively safer result. Therefore, we did not further adjust the damping ratio. Based on the above results, the parameters of the aero-elastic model were calculated and are shown in Table 4.

2.3 Wind profile

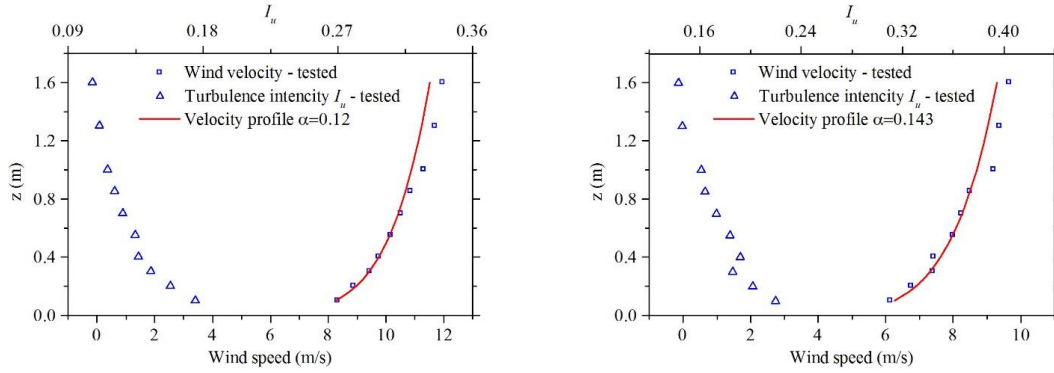
The terrain at the location of the high lighting pole is open and flat and considered a Class A environment in the China code (CABR 2012). This test was conducted in a boundary layer wind tunnel at Zhejiang University. The test simulated Class A flow per the China code; typhoon flow and uniform flow were also simulated. The typhoon profile was suggested by Sharma (Sharma and Richards 1999).

Table 3 Vibration test results for the first damping ratio.

Test number	First-mode damping ratio (acceleration)	First-mode damping ratio (shear force)	First-mode damping ratio (bending moment)
X-1	0.31%	0.32%	0.27%
X-2	0.32%	0.33%	0.32%
X-3	0.36%	0.36%	0.32%
Y-1	0.29%	0.31%	0.29%
Y-2	0.33%	0.39%	0.32%
Y-3	0.27%	0.29%	0.30%
Average	0.32%	0.33%	0.30%

Table 4 Similarity parameters of the aero-elastic model

Parameters	Scale	Similarity relationship
Geometry	1:25	f_L
Natural frequency	5.15:1	f_ω
Wind speed	1:4.85	$f_V = f_L / f_\omega$
Acceleration	1.063:1	$f_A = f_L \times f_\omega^2$
Base moment	1:367539	$f_M = f_V^2 \times f_L^3$
Base shear force	1:14701	$f_F = f_V^2 \times f_L^2$



(a) Profile of class A terrain flow in the China code

(b) Profile of typhoon flow.

Fig. 6 Simulated wind profile

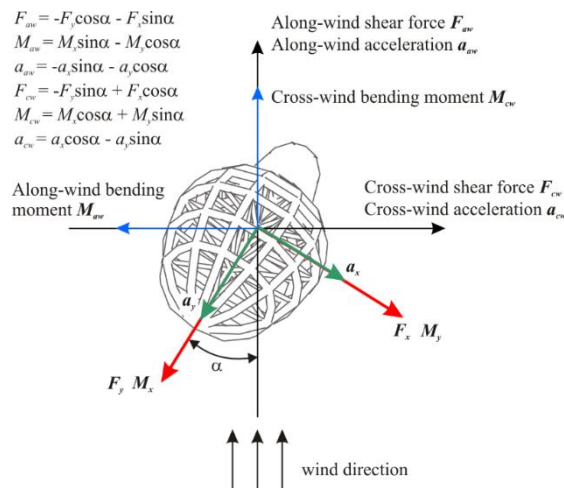


Fig. 7 Decomposition of measured data in X and Y directions into along-wind and cross-wind response.

The wind speed profile of typhoon flow followed the exponential law, and the turbulence intensity was Class A field turbulence intensity multiplied by a factor of 1.60. The profiles of Class A flow and typhoon flow are shown in Fig. 6.

3. Analysis of test results

To calculate the along-wind and cross-wind response, the basement force response and acceleration response in the X and Y directions were decomposed into along-wind and cross-wind directions. Because the force balance and acceleration sensor systems had different coordinate systems, the decomposition methods of bending moment, shear force and acceleration were different. The decomposition equations are listed in Fig. 7; the direction of the bending moment

vector follows the right-hand rule.

The load code of China specifies that the basic design wind pressures for a 10-year period, 50-year period and 100-year period in Zhoushan shall be 0.5 kN/m², 0.85 kN/m² and 1.0 kN/m², respectively. Based on Eq. (4) and the wind speed scale in Table 4, the corresponding design wind speeds at a height of 40 cm (equivalent to a 10 m height in the real structure) in the test were 5.84 m/s, 7.62 m/s and 8.26 m/s, respectively. Analysis in this paper focuses primarily on the response under these three test wind speeds.

$$w_0 = \frac{1}{2} \rho v_0^2 \approx \frac{1}{1600} v_0^2 \quad (4)$$

3.1 Analysis of along-wind response

The mean value and standard deviation of bending moment and shear force under different design wind speeds are shown in Fig. 8. The bending moments and shear forces were converted into full-scale data. The mean result reaches minimum when wind direction is 90°, where the windward area is the smallest. However, the standard deviation which represents the dynamic response of the structure, has the largest value at a 150° wind direction.

Since the mean response is mainly related to windward area, the following content will only focus on dynamic vibration response. In order to study the vibration response in detail, the power spectrum of the along-wind bending moment response at a 150° wind direction was analyzed and is shown in Fig. 9. The power spectrum shape at different wind speeds is relatively similar. At the design wind speed, the first-order vibration component was dominant. To explore the relations between resonance components and background components, the integrals of the first- and second-order resonance response power spectrum densities were computed. The integral values were the first and second-order resonance components. Then, the background components were calculated by subtracting these resonance components from the total energy as follows

$$\lambda_{v1} = \frac{\int_{f_{1s}}^{f_{1e}} S_d(n) dn}{\int_0^{+\infty} S_d(n) dn} \quad (5)$$

$$\lambda_{v2} = \frac{\int_{f_{2s}}^{f_{2e}} S_d(n) dn}{\int_0^{+\infty} S_d(n) dn} \quad (6)$$

$$\lambda_b = 1 - \lambda_{v1} - \lambda_{v2} \quad (7)$$

Fig. 10 represents how the proportion of the background component and the resonant component changed with wind speeds at a 150° wind direction. The proportion of first-order vibration in the wind fluctuation response gradually increased with increasing wind speed; when the wind speed was greater than 4.8 m/s, the proportion of first-order vibration grew to more than 90% and then remained at this level. Therefore, the first-order resonant vibration is the main component of along-wind vibration under the design wind speed.

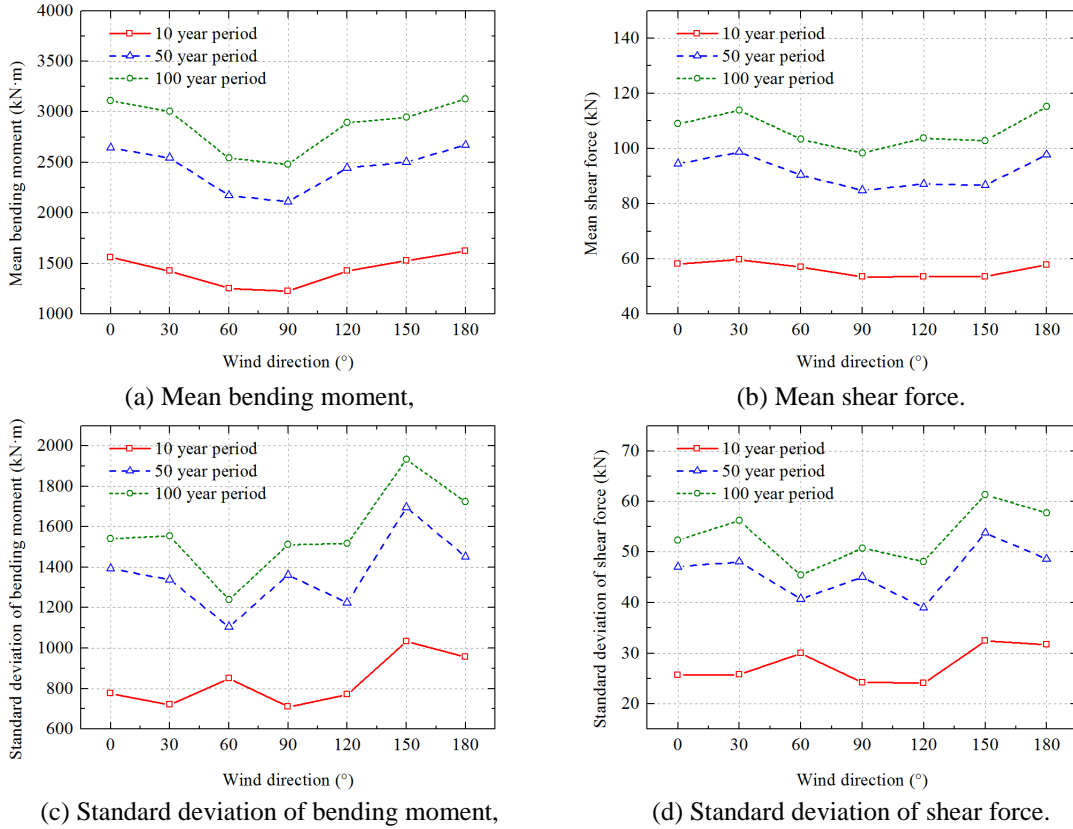


Fig. 8 Mean value and standard deviation of along-wind response under design wind speed

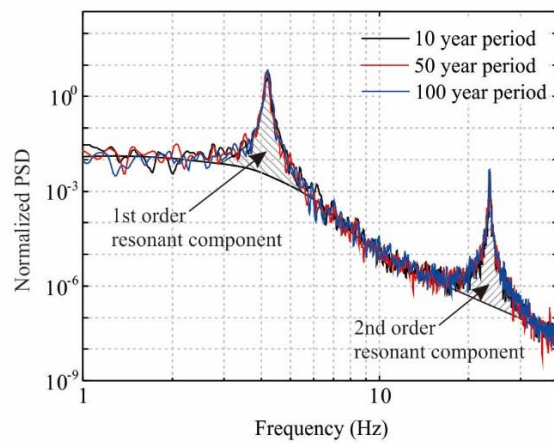


Fig. 9 Power spectrum of along-wind bending moment under different design wind speeds.

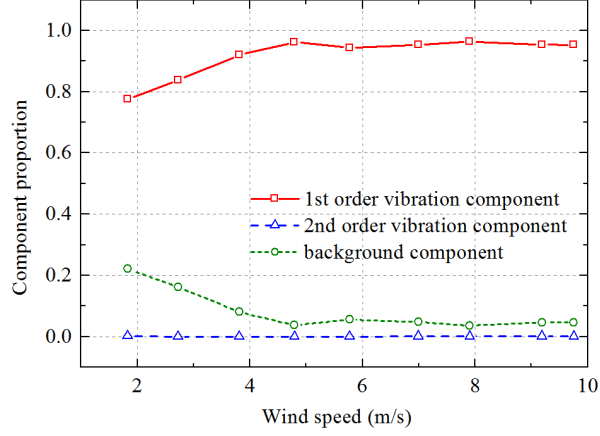


Fig. 10 Proportion of each component in along-wind bending moment response under different wind speeds in a 150° wind direction

3.2 Analysis of along-wind wind-induced vibration coefficient

According to China load code, wind force on structures could be calculated by Eq. (8)

$$w_k = \beta_z \mu_s \mu_z w_0 \quad (8)$$

where w_0 is the basic velocity pressure, $\mu_s \mu_z$ is the pressure coefficient represent the shape and height influence on pressure distribution, β_z is the wind-induced vibration coefficient which represents the magnification effect of wind-induced response. In order to study the relationship between along-wind dynamic response and mean response, this section will focus on wind vibration coefficient of this structure.

3.2.1 Coefficient in China code

In the China load code, the vibration coefficient is calculated by the inertial wind load method. According to random vibration theory, for a general vertical cantilever structure, the wind vibration coefficient β_z at a height z is calculated by Eq. (9)

$$\beta_z = 1 + 2gI_{10}B_z \sqrt{1 + R^2} \quad (9)$$

where I_{10} is the turbulence intensity at 10 m height, B_z is the background factor of the dynamic wind load, and R is the resonance factor of the dynamic wind load. Strictly speaking, Eq. (9) can only calculate the wind vibration coefficient of structures with uniform shape and weight distribution. The lighting pole in this study features prominent vertical changes in shape and weight. To study the specific influence of these changes on the wind vibration coefficient, we started from random vibration theory and calculated the coefficient by considering uneven weight distributions and cross-sectional area changes. The vibration coefficient of high-rise structures is calculated by Eq. (10)

$$\beta_z = 1 + \xi \varepsilon_1 \varepsilon_2 \quad (10)$$

where ξ is a dynamic amplification factor caused by structure resonance that is equal to the background component in the code method; ε_1 is the spatial correlation coefficient of the wind pressure; and ε_2 is a factor related to the shape and weight distribution. ξ , ε_1 and ε_2 were calculated by Eqs. (11)-(13)

$$\xi = \sqrt{\omega_1^4 \int_0^\infty S_1(n) |H_1(i\omega)|^2 d\omega} \quad (11)$$

$$\varepsilon_1 = \frac{\sqrt{\int_0^B \int_0^B \rho_{x_1 x_2} dx_1 dx_2 \int_0^H \int_0^H \mu_s(z_1) \mu_z(z_1) \mu_f(z_1) A(z_1) \phi_1(z_1) \mu_s(z_2) \mu_z(z_2) \mu_f(z_2) A(z_2) \phi_1(z_2) \rho_{z_1 z_2} dz_1 dz_2}}{\int_0^H m(z) \phi_1^2(z) dz} \quad (12)$$

$$\varepsilon_2 = \frac{m(z) \phi_1(z)}{\mu_s(z) \mu_z(z) A(z)} \quad (13)$$

where $\mu_f(z)$ is the turbulence dynamic factor calculated by Eq. (14)

$$\mu_f(z) = 2gI(z) \quad (14)$$

where $I(z)$ is the turbulence intensity at height z , g is a peak factor equal to 2.5 in the China code, μ_s, μ_z is same as Eq. (9). Because the shape coefficient of this lighting pole could not be found in any code, we used the overall shape coefficient μ_s to simplify the calculation. The overall shape coefficient can be calculated based on experimental results for uniform flow. During uniform flow, the average drag coefficient is equal to the shape coefficient in Eq. (15)

$$\mu_s = \bar{C}_D(\alpha) = \frac{\bar{F}_D(\alpha)}{\bar{q}_H A_{rif}} \quad (15)$$

where $\bar{F}_D(\alpha)$ is the average bottom shear force under uniform flow in wind direction α , \bar{q}_H is the average wind pressure calculated by wind speed, and A_{rif} is the overall windward area. The overall shape coefficient in different wind directions is between 0.85 and 0.95. Since the change range is relative small, thus the overall shape coefficient was finally set to 0.9. To avoid multiple integration in Eq. (12), the structure could be simplified as a cantilever structure with multiple mass points; every mass point had a certain windward area and a certain mass. Therefore, Eq. (12) was converted into the sum of the factors calculated at each point, and the result was 0.93.

Because wind vibration coefficients in different wind directions were similar, we analyzed only the coefficients for the 0° wind direction. Two parameters (B_z and ε_2) were calculated at each mass point in the z direction. Wind vibration coefficients were calculated by Eqs. (9) and (10) as β_z and $\beta_{z,1}$, respectively. The two coefficients and parameters B_z and ε_2 are shown in Fig. 11.

$\beta_{z,1}$ exhibited a prominent change at a height of 30 m and increased sharply at the top of the structure because windward area and weight sharply decreased at the top of the structure, which caused a lash effect that resulted in the larger coefficient. This means that the wind vibration coefficient calculated by the second method better matched reality.

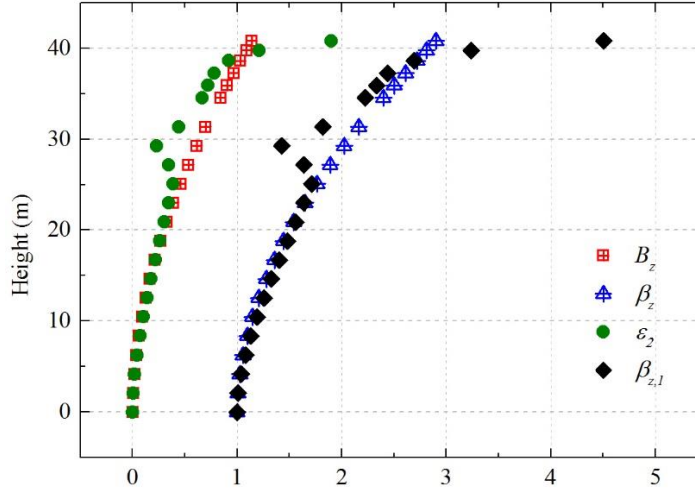


Fig. 11 Results of the wind vibration coefficient calculated according to the China code

To compare with the experiment results, the coefficients β_z and $\beta_{z,l}$ needed to be averaged with the area-weighted approach of Eq. (16)

$$\bar{\beta}_z = \frac{\sum \beta_{zi} \mu_{si} \mu_{zi} A_i}{\sum \mu_{si} \mu_{zi} A_i} \quad (16)$$

where $\bar{\beta}_z$ represents the overall wind vibration coefficient. The wind vibration coefficient calculated by the first method was 1.99 and that by the second method was 1.93. The second calculation method considered changes of the shape of the weight; however, the wind vibration coefficient was still close to the calculation results based on the China code, which means that the shape and weight distribution had a limited influence on this structure and that the wind vibration coefficient directly calculated by the code was feasible.

3.2.2 Coefficient in Eurocode

In order to strengthen the result, Eurocode was also taken into consideration. According to Eurocode, wind forces on whole structure or a structural component should be calculated by Eq. (17)

$$F_w = c_s c_d \cdot c_f \cdot q_p(z_e) \cdot A_{ref} \quad (17)$$

where $q_p(z_e)$ is the peak velocity pressure at reference height z_e , c_f is the force coefficient. $c_s c_d$ is the structural factor represents the effect of peak wind pressure and effect of the structural vibration due to the turbulence. This coefficient has similar meaning with wind vibration coefficient β_z in China code. $c_s c_d$ was calculated by Eq. (18)

$$c_s c_d = \frac{1 + 2 \cdot k_p \cdot I_v(z_e) \cdot \sqrt{B^2 + R^2}}{1 + 7 \cdot I_v(z_e)} \quad (18)$$

where k_p is the peak factor, I_v is the turbulence intensity, B^2 is the background factor, R^2 is the resonance response factor. In order to compare with China code and experiment result, the peak velocity pressure q_p should be transfer into basic velocity pressure. Thus the structural factor turned into Eq. (19)

$$c_s c_d' = 1 + 2 \cdot k_p \cdot I_v(z_e) \cdot \sqrt{B^2 + R^2} \quad (19)$$

The calculation result of above-mentioned parameters was listed in Table 5. In order to compare with the experiment results, the structural factor was also averaged with the area-weighted approach. The average structural factor was 2.78 which is larger than coefficient in China code. This is because the peak factor according to Eurocode is 3.66, which is much greater than that in China code.

3.2.3 Experiment result

Because the bottom shear force was equal to the total surface wind load on the structure, the wind vibration coefficient of the bottom shear force was equivalent to the overall wind vibration coefficient analyzed above. The wind vibration coefficient of the shear force was calculated by Eq. (20)

$$\bar{\beta}_{F_d} = \frac{F_{d,\max}}{\bar{F}_d} \quad (20)$$

Table 5 Parameters of structural factor according to Eurocode

Parameters	Result	Calculation formula
k_p	3.66~3.67	$k_p = \sqrt{2 \cdot \ln(v \cdot T)} + \frac{0.6}{\sqrt{2 \cdot \ln(v \cdot T)}}$
I_v	0.10~0.17	$I(z) = \frac{k_1}{c_o(z) \cdot \ln(z/z_0)}$
B^2	0.50~0.71	$B^2 = \frac{1}{1 + 0.9 \cdot \left(\frac{b+h}{l(z_e)}\right)^{0.63}}$
R^2	3.47~3.84	$R^2 = \frac{\pi^2}{2 \cdot \delta} \cdot S_L(z_e, n_{1,x}) \cdot R_h(\eta_h) \cdot R_b(\eta_b)$
$c_s c_d'$	2.61~3.52	$c_s c_d' = 1 + 2 \cdot k_p \cdot I_v(z_e) \cdot \sqrt{B^2 + R^2}$

The wind vibration coefficients of the shear force at 0° wind direction with different wind speeds were calculated by Eq. (16) and are shown in Fig. 12. The wind vibration coefficient slightly decreased with increasing wind speed; the average wind vibration coefficient was 2.35, which was bigger than the result based on the China code and was smaller than that in Eurocode. This difference may be caused by different peak factors. In the wind tunnel test, the calculation method of the peak factor of bottom shear force is given by Eq. (21)

$$g_F = \frac{F_{d,\max} - \bar{F}_d}{\sigma_{F_d}} \quad (21)$$

This parameter reflects the distribution of structural dynamic response. The peak factor of the bottom shear force at a 0° wind direction with different wind speeds is also shown in Fig. 12. The peak factor was relatively stable with the change of wind speed. The mean value of the peak factor was 3.47, much larger than the value in the China code of 2.5. However, it was close to peak factor in Eurocode which is 3.67. By changing the peak factor in Eqs. (9) and (14) from 2.5 to 3.5, the recalculated overall wind vibration coefficients were 2.40 and 2.30, respectively. These results not only agree well with the test result of 2.35 but also get close to result of Eurocode, which demonstrates that during wind vibration coefficient calculation, China code underestimated the peak factor, the peak factor in the formula need be changed into 3.5 to encompass the dynamic response of the structure. Eurocode estimate the peak factor more accurately than China, but it has a slight overestimation of the wind vibration coefficient, which is safer for real structure design.

To further explore the wind vibration coefficient of this structure during different flow fields, we enveloped all wind vibration coefficients of the bottom shear force under different wind directions and compared the coefficients in Class A flow and typhoon flow with different wind speeds. The results are shown in Fig. 13. The populated areas between the error lines in the figure represents the envelope area of the wind vibration coefficient under different wind directions. When the wind speed was small, the coefficients dispersed greatly under different wind directions, and the coefficients in typhoon flow were greater than the wind vibration coefficients in Class A flow. When the wind speed increased gradually, the differences gradually decreased, and the coefficients in typhoon flow became much larger than the coefficients in Class A flow. This result demonstrates that high turbulence flow has a strong influence on the structure's along-wind wind vibration coefficients. However, per the China code, wind vibration coefficients in different areas were calculated with the same equation, which is clearly not safe for certain typhoon-prone areas such as Zhoushan. Therefore, based on the test results, we suggest that for structures in typhoon-prone areas, the along-wind wind vibration coefficient should be multiplied by an extra magnification coefficient of 1.6 on the basis of the wind vibration coefficient calculated by the China code to ensure the safety of structures in high turbulence situations.

3.3 Analysis of cross-wind response

Cross-wind loads may cause strong wind resonance under critical Reynolds number flow because the cross section of the column is circular and the design wind speed is in a critical area. However, since coupling of modes in orthogonal planes exists on this structure, along-wind response will give rise to a component of cross-wind response, therefore the cross-wind response of this structure might have difference with theoretical analysis.

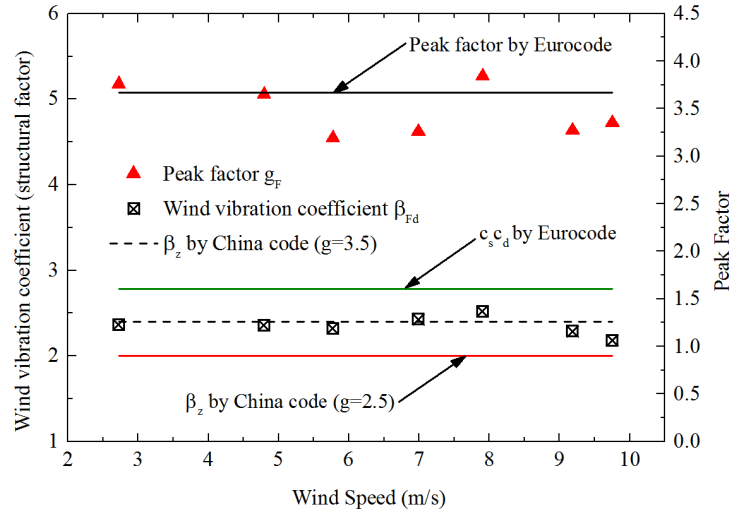


Fig. 12 Wind vibration coefficients of bottom shear force and coefficients by the China code and Eurocode for 0° wind direction with different wind speeds

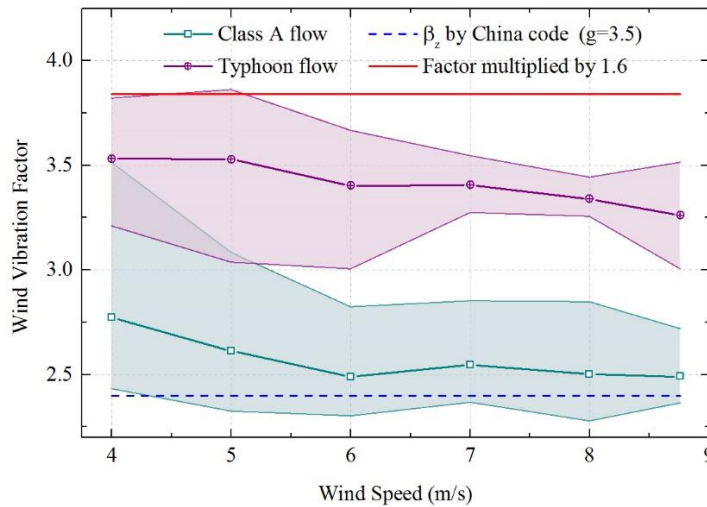


Fig. 13 Wind vibration coefficients of shear force in different wind flow fields.

Fig. 14 shows the standard deviation values of the cross-wind shear force as a function of mean wind velocity in different wind directions. The three component proportions were calculated by Eqs. (5)-(7) as was done in the along-wind analysis. Using standard deviation values of the cross-wind shear force times these three component proportions, we could figure out values of each component. The changing patterns with wind velocity under different wind directions were similar. With increasing wind speed, the first-order resonance gradually moved into the main position. Next, when wind speed gradually increased to the design wind speed, the vibration mode

gradually changed from first-order vibration to second-order vibration. Then, when wind velocity continued to rise, the second-order resonant component reached a peak and then started to decrease in most wind directions. Fig. 15 shows the power spectrum of the cross-wind shear force under different wind speeds under 120° wind direction. The vortex shedding frequency increased with wind speed. When the wind speed reached 7.90 m/s, the vortex frequency and second-order natural frequency became equal, which implies the occurrence of the second-order vortex-induced resonance phenomenon.

In order to investigate difference between test result and equivalent wind load during design, comparison with Eurocode cross-wind response was proceeded. According to Eurocode, the critical wind velocity for mode i was defined in Eq. (22). In order to compare the Eurocode result with test result more reasonably, the wind speed calculated in Eurocode were all scaled into test speed with a scale of 4.85:1.

$$v_{crit,i} = \frac{b \cdot n_{i,y}}{St} \quad (22)$$

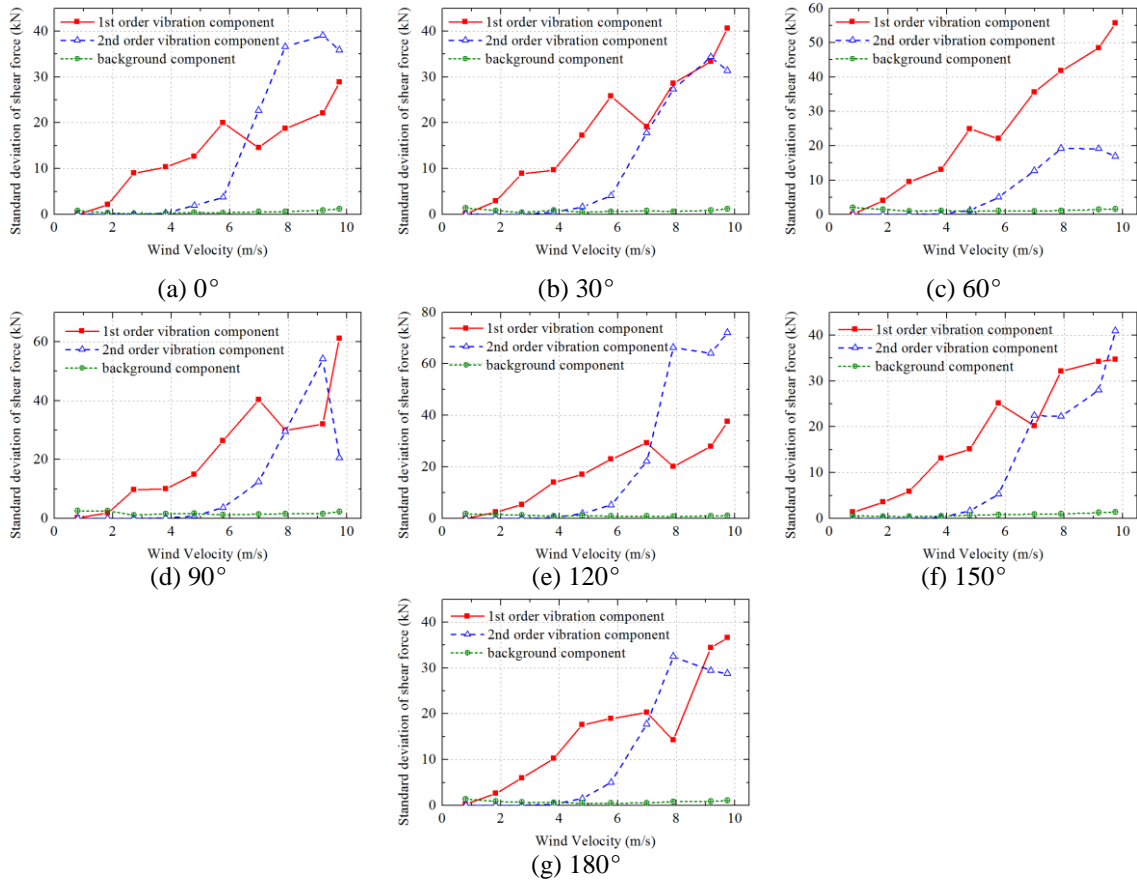


Fig. 14 Standard deviation of each component in cross-wind response under different wind speeds

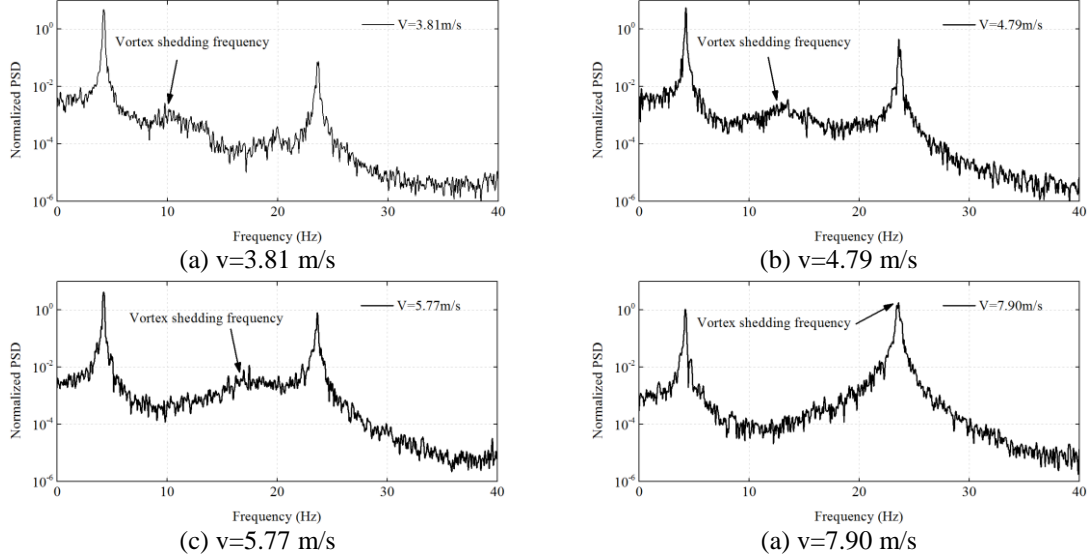


Fig. 15 Power spectrum of cross-wind shear force at 120° wind direction ($v=3.81\text{-}7.90\text{ m/s}$)

where b is the reference width of the cross-section at which resonant vortex shedding occurs, $n_{i,y}$ is the structural natural frequency, St is the Strouhal number. The reference width of this structure varied from 1.33 m to 1.58 m. The first and second-order natural frequency is 0.817 Hz and 4.35 Hz, respectively. The Strouhal number for circular cross-section is 0.18. Thus the first and second-order critical wind velocity after scaling are 1.25 m/s~1.48 m/s and 6.66 m/s~7.87 m/s, respectively. The second order critical wind velocity was perceived by test result, but the first critical velocity was so small that it cannot input enough energy to the structure to create resonant vibrations. Thus, it can be reasonably considered that the first order vibration component in the test result was not resulting from the first-order crosswind resonance, it mainly came from the first-order along-wind vibration due to the coupling effect between two orthogonal modes.

The design wind velocity at the structure top with 50 years return period was 43.54 m/s in real scale. Thus the corresponding scaled wind velocity was 8.97 m/s. The critical velocity of first two modes were below 1.25 times of the design wind velocity of this structure, thus checking calculation for cross-wind vortex shedding vibration is needed according to Eurocode. The cross-wind vibration due to vortex shedding was calculated by Eqs. (23) and (24)

$$F_w(s) = m(s) \cdot (2 \cdot \pi \cdot n_{i,y})^2 \cdot \Phi_{i,y}(s) \cdot y_{F,\max} \quad (23)$$

$$\frac{y_{F,\max}}{b} = \frac{1}{St^2} \cdot \frac{1}{Sc} \cdot K \cdot K_w \cdot c_{lat} \quad (24)$$

where St is the Strouhal number, Sc is the Scruton number. Since Eurocode considered the influence of mass distribution, vibrations effect induced by vortex shedding was calculated in 2 circumstances and compared afterwards: 1. mass is uniform distributed, 2. mass distribution is same as FEM model.

Fig. 16 is first-order and second-order cross-wind vibration effect on different height of this structure. After considering uneven mass distribution, the wind effect concentrated more on lamp part. Therefore the connection between the lampshade and the pole and the middle part of lampshade will subjected to larger bending moment and shear force.

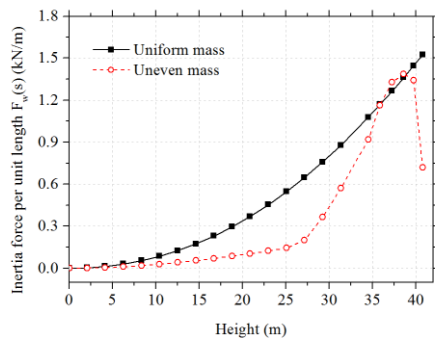
Then the basement shear force was calculated by integration of wind effect in different height, the result was compared with test result as shown in Table 6. The first-order and second-order shear force in the test were calculated by Eq. (25).

$$F_{eq,2} = g \cdot \sigma_F \quad (25)$$

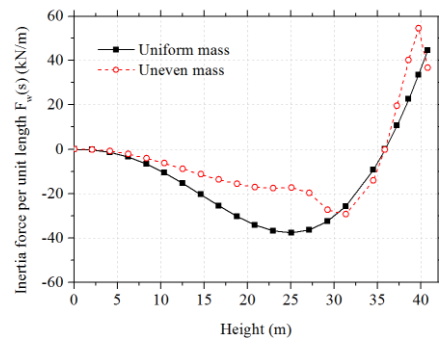
where g equals 3.0, σ_F is standard deviation of first-order and second-order resonant component. The test result in the comparison was calculated when wind direction equals 120° , where the second-order component response was the largest as shown in Fig. 14(e). After considering the uneven mass, the first-order and second-order basement shear force significantly decreased. However, the first-order result based on Eurocode was smaller than test result, and the second-order result was still larger than test result. The difference of first order result verified the conclusion before, that this structure had a coupling effect in perpendicular planes, the along-wind response will give rise to cross-wind response. The difference of second order result may because Eurocode only take mass distribution into consideration, but the lampshade on the top was hollowed and had plenty of gaps between lamps, which would cause local turbulence and decrease the wind-induced vibration. Therefore, Eurocode overestimated the second-order resonant vibration for this structure but was on the safe side during wind load design.

Table 6 Comparison of basement shear force between Eurocode and wind tunnel test

	Eurocode (uniform mass)	Eurocode (uneven mass)	Test result ($\alpha=120^\circ$, $v=7.90$ m/s)
First-order basement shear force (kN)	20.07	13.18	60.44
Second-order basement shear force (kN)	598.00	294.48	198.97



(a) First-order



(b) Second-order

Fig. 16 Equivalent cross-wind load distribution based on Eurocode

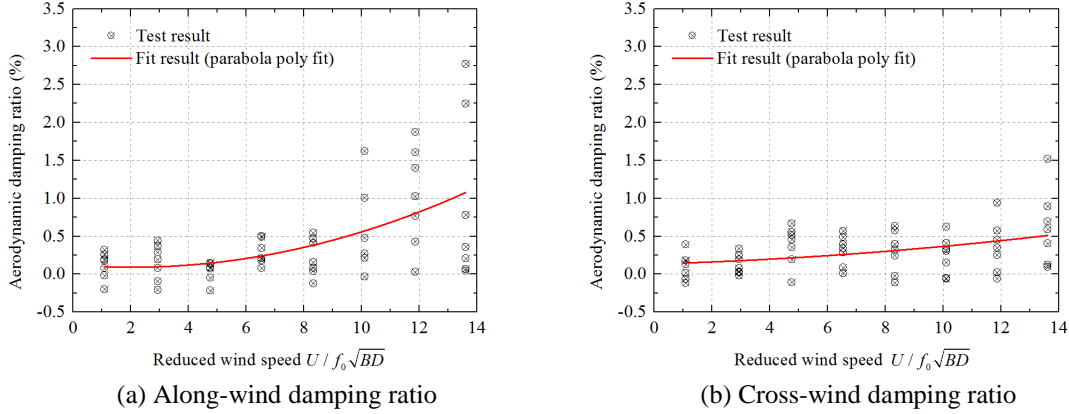


Fig. 17 Identification results of aerodynamic damping ratio

3.4 Aerodynamic instability analysis

Because of fluid-structure coupling, there may be additional aerodynamic stiffness, aerodynamic mass and aerodynamic damping when a structure is vibrating in a flow field (Simiu and Scanlan 1996). For high-rise steel structures, the influence of the first two parameters are relatively small; for small damping steel structures, aerodynamic damping has a large impact on the vibration response of a structure. In this study, random decrement technique (Ibrahim 1977) was used to further process the acceleration time history of structural vibration and then identify the aerodynamic damping of the structure. The random decrement technique (RDT) is a simple and efficient method to estimate the first-order damping ratio of a high-rise structure (Marukawa *et al.* 1996).

The RDT method requires a large quantity of signal points, which means that the sample time should be relatively long; research shows that the number of analyzed segments should be at least 5,000 to obtain satisfactory results (Tamura and Suganuma 1996). However, the test time of this wind tunnel experiment was limited, and the damping ratio results may contain some errors. The aerodynamic damping ratio calculation formula is Eq. (26)

$$\zeta_a = \zeta - \zeta_s \quad (26)$$

where ζ is the overall damping ratio of structure and ζ_s is the structural natural vibration damping ratio. Fig. 17 shows the along-wind aerodynamic damping and cross-wind aerodynamic damping under different wind speeds. In the figure, the X axis is the reduced wind speed, U is the test wind speed, f_0 is the first-order natural frequency, B is the windward width, and D is the along-wind length. With the increase of reduced wind speed, along-wind aerodynamic damping ratios and cross-wind aerodynamic damping ratios both had a slowly increasing trend. When reduced wind speed is larger than 10, along-wind result became discrete while cross-wind result was still centralized. Moreover, the magnitude of along-wind aerodynamic damping was slightly larger than cross-wind result, which had an accordance with quasi-steady theoretical result (Solari and Pagnini 1999). However, since the lampshade is asymmetric and the RDT has error when test time is limited, test result cannot give a determined value or function of aerodynamic damping, the

increase trend in Fig. 17 was just for reference. Only one conclusion could be obtained: this structure is asymptotically stable and will not have aerodynamic instability problems at design wind speed. This provides a reference for aerodynamic instability decisions during the design of similar structures.

4. Conclusions

In this study, an aero-elastic model wind tunnel test of a 40 m lighting pole was conducted, and wind-induced responses under different wind speeds, different wind directions and different flow fields were analyzed. Some useful conclusions are as follows:

For structures whose two perpendicular-direction natural frequencies are relatively close, a beat phenomenon easily occurs in free vibration testing. To identify the natural damping ratio of these structures, vibration in two directions should be synthesized as vectors. The damping ratio identification result of the model in this study was 0.0032, which is less than the damping ratio of steel structures in the China code (0.01). However, the result agrees well with the U.S. code and the Europe code, and the test results are expected to be more robust.

The along-wind dynamic bending moment and dynamic shear force of the structure varied similarly in different wind directions. When the wind speed increased, the first-order resonance component gradually dominated the dynamic response.

The wind vibration coefficient calculated by the China code was similar to that calculated by the random vibration method when the uneven distribution of weight and windward area was considered. The overall wind vibration coefficient by the China code was 1.99, less than the average wind vibration coefficient of the shear force during the test (2.36). When the peak factor in the code was replaced by the test result of 3.5, the wind vibration coefficient according to the China code became 2.40, which is close to the experimental value. Eurocode estimate the peak factor more accurately than China, but it has a slight overestimation of the wind vibration coefficient, which is safer for real structure design. Based on the comparison of different flow field test results, it is suggested that to ensure the safety of structures under the action of typhoons in typhoon-prone areas we require an extra amplification coefficient of 1.6 for the along-wind wind vibration coefficient estimation of similar high-rise structures.

The changing patterns of cross-wind response with wind velocity under different wind directions were similar. By analyzing the cross-wind response power spectrum, it can be concluded that the second-order vortex-induced resonance phenomenon occurred at high wind speeds, which caused dynamic shear forces to greatly increase. By comparing the test result with Eurocode, some conclusions were obtained: After considering uneven mass distribution, the wind effect concentrated more on lamp part, thus the connection between the lampshade and the pole and the middle part of lampshade will subjected to larger bending moment and shear force while the first-order and second-order basement shear force significantly decreased. Eurocode overestimated the second-order resonant vibration for this structure but was on the safe side during wind load design.

The aerodynamic damping ratio was identified using the random decrement method. The distribution of the damping ratio with reduced wind speed was analyzed. The along-wind identification results were discrete, but overall values showed a trend of a slow increase. Under design wind speed, aerodynamic damping ratios were mostly positive, which demonstrates that the structure would not have aerodynamic instability problems.

Acknowledgments

The research presented in this paper was financially supported by the 13th Five-Year national key research under project No.2016YFC0800206, which is gratefully acknowledged.

References

- ASME (2006), *Steel Stacks*, The American Society of Mechanical Engineers, New York.
- Belloli, M., Rosa, L. and Zasso, A. (2014), “Wind loads on a high slender tower: numerical and experimental comparison”, *Eng. Struct.*, **68**, 24-32.
- Belver, A.V., Ibán, A.L. and Lavín Martín, C.E. (2012), “Coupling between structural and fluid dynamic problems applied to vortex shedding in a 90m steel chimney”, *J. Wind Eng. Ind. Aerod.*, **100**(1), 30-37.
- CABR (2012), *Load Code for the Design of Building Structures*, China Academy And Building Research, Beijing.
- Caracoglia, L. (2007), “Influence of weather conditions and eccentric aerodynamic loading on the large amplitude aeroelastic vibration of highway tubular poles”, *Eng. Struct.*, **29**(12), 3550-3566.
- Caracoglia, L. and Jones, N.P. (2007), “Numerical and experimental study of vibration mitigation for highway light poles”, *Eng. Struct.*, **29**(5), 821-831.
- Caracoglia, L. and Velazquez, A. (2008), “Experimental comparison of the dynamic performance for steel, aluminum and glass-fiber-reinforced-polymer light poles”, *Eng. Struct.*, **30**(4), 1113-1123.
- Chen, X., Li, A., Wang, Y. and Zhang, Z. (2014), “Comparative study on equivalent wind loads and dynamic responses of self-standing high-rise structures in different codes”, *J. Build. Struct.*, **4**, 304-311.
- Eurocode (2006), *Design of Steel Structures: Part 3-2: Towers, Masts and Chimneys*, European Committee for Standardization, Brussels, Belgium.
- Fediw, A.A., Nakayama, M., Cooper, K.R., Sasaki, Y., Resende-Ide, S. and Zan, S.J. (1995), “Wind tunnel study of an oscillating tall building”, *J. Wind Eng. Ind. Aerod.*, **57**(2), 249-260.
- Gorski, P. (2009), “Some aspects of the dynamic cross-wind response of tall industrial chimney”, *Wind Struct.*, **12**(3), 259-279.
- Gu, M. and Quan, Y. (2004), “Across-wind loads of typical tall buildings”, *J. Wind Eng. Ind. Aerod.*, **92**(13), 1147-1165.
- Ibrahim, S.R. (1977), “Random decrement technique for modal identification of structures”, *J. Spacecraft Rockets.*, **14**(11), 696-700.
- Kawecki, J. and Żurański, J.A. (2007), “Cross-wind vibrations of steel chimneys—a new case history”, *J. Wind Eng. Ind. Aerod.*, **95**(9-11), 1166-1175.
- Marukawa, H., Kato, N., Fujii, K. and Tamura, Y. (1996), “Experimental evaluation of aerodynamic damping of tall buildings”, *J. Wind Eng. Ind. Aerod.*, **59**(2-3), 177-190.
- Nguyen, C.H., Freda, A., Solari, G. and Tubino, F. (2015), “Aeroelastic instability and wind-excited response of complex lighting poles and antenna masts”, *Eng. Struct.*, **85**, 264-276.
- Nguyen, C.H., Freda, A., Solari, G. and Tubino, F. (2015), “Experimental investigation of the aeroelastic behavior of a complex prismatic element”, *Wind Struct.*, **20**(5), 683-699.
- Pagnini, L.C. and Solari, G. (2001), “Damping measurements of steel poles and tubular towers”, *Eng. Struct.*, **23**(9), 1085-1095.
- Repetto, M.P. and Solari, G. (2010), “Wind-induced fatigue collapse of real slender structures”, *Eng. Struct.*, **32**(12), 3888-3898.
- Rosa, L., Tomasini, G., Zasso, A. and Aly, A.M. (2012), “Wind-induced dynamics and loads in a prismatic slender building: A modal approach based on unsteady pressure measurements”, *J. Wind Eng. Ind. Aerod.*, **107-108**, 118-130.
- Sharma, R.N. and Richards, P.J. (1999), “A re-examination of the characteristics of tropical cyclone winds”, *J. Wind Eng. Ind. Aerod.*, **83**(1-3), 21-33.

- Simiu, E. and Scanlan, R.H. (1996), *Wind Effects on Structures*, Wiley
- Solari, G. and Pagnini, L.C. (1999), "Gust buffeting and aeroelastic behaviour of poles and monotubular towers", *J. Fluids Struct.*
- Tamura, Y. and Suganuma, S. (1996), "Evaluation of amplitude-dependent damping and natural frequency of buildings during strong winds", *J. Wind Eng. Ind. Aerod.*, **59**(2-3), 115-130.
- Verboom, G.K. and Van Koten, H. (2010), "Vortex excitation: three design rules tested on 13 industrial chimneys", *J. Wind Eng. Ind. Aerod.*, **98**(3), 145-154.
- Zhou, Y., Kijewski, T. and Kareem, A. (2002), "Along-wind load effects on tall buildings: comparative study of major international codes and standards", *J. Struct. Eng. - ASCE*, **128**(6), 788-796.

CC